View Article Online
View Journal

Nanoscale

Accepted Manuscript

This article can be cited before page numbers have been issued, to do this please use: L. Chabeaud, N. F. Barrera, J. Contreras-Garcia, J. Lam and H. Guesmi, *Nanoscale*, 2026, DOI: 10.1039/D6NR01396A.

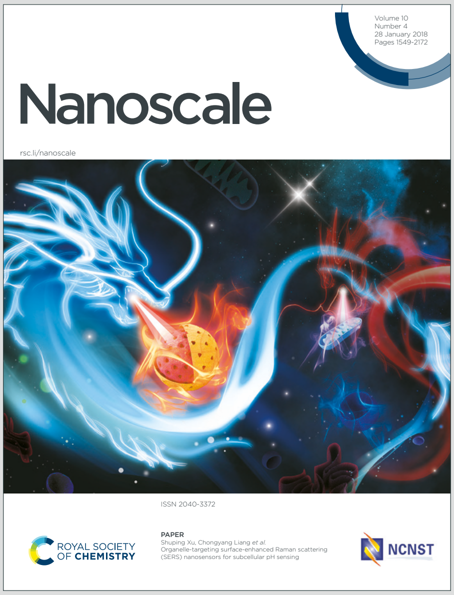

ROYAL SOCIETY
OF CHEMISTRY

rsc.li/nanoscale

View Article Online
DOI: 10.1039/D6NR01396A

Hydrogen‑Directed Au–H–Au Chain Networks Redefine the Active Structure of Sub‑2 nm Gold Nanoparticles

Loréna Chabeaud[1],
Nicolás F. Barrera[2], Julia Contreras-García[2], Julien Lam[3] and Hazar Guesmi[1*]

[1] ICGM, UMR 5253, Univ Montpellier, CNRS, ENSCM, Montpellier, France

[2] Laboratoire de Chimie Théorique, Sorbonne Université and CNRS, 4 Pl Jussieu, F-75005, Paris, France

[3] Université Lille, Centre National de la Recherche Scientifique, INRA, ENSCL, UMR 8207, UMET, Unité Matériaux et Transformations, 59000 Lille, France

AUTHOR INFORMATION
hazar.guesmi@umontpellier.fr

Abstract

Under H_2, sub-2 nm Au nanoparticles are highly fluxional and evade static coordination-based descriptions. Using DFT and 300 K ab-initio molecular dynamics, we track hydrogenation of icosahedral Au_{147} and truncated-octahedral Au_{201} from ideal adsorption motifs to thermally reconstructed, dynamically sampled structures. Near-monolayer hydrogen acts as a structure-directing reactant, reorganizing the outer shell into contracted Au–H–Au chain networks while sustaining a fluctuating population of adsorbate-induced unusual low-coordination Au sites. Electronic descriptors reconcile hydride-like polarity with metallic character: hydrogen becomes negatively charged whereas gold is positively polarized, yet the density of states remains finite at the Fermi level. ELF connectivity and saddle-point analysis of the hydrogenated gold nanoparticles reveal the emergence of a delocalized, heterogeneous electronic network in the reconstructed state, able to redistribute charge and mediate hydrogen transfer. Calculated IR features at 2000–2160, 1780, and 1630–1680 cm^{-1} rationalize debated operando band assignments. In ethene hydrogenation, Au–H–Au chain ensembles weaken the driving force for successive hydrogen additions by disrupting stabilizing bridging motifs, providing a mechanistic basis for the high selectivity of ultrasmall Au catalysts.

View Article Online
DOI: 10.1039/D6NR01396A

I. Introduction

Gold is often regarded as chemically inert in its bulk form, yet it displays strikingly different behavior when dispersed into nanoscale particles. Since Haruta's seminal discovery of supported Au nanoparticles (NPs) as highly active catalysts for low-temperature CO oxidation [1-2], extensive work has established that Au becomes catalytically effective once its size decreases into the few-nanometer regime, with activity frequently increasing as particle size decreases [3-7]. In hydrogen-rich environments, Bond and co-workers further showed that ultrasmall Au NPs that chemisorb H_2 promote hydrogenation reactions, whereas larger particles remain comparatively hydrogen-poor and substantially less active [8]. Together, these observations establish sub-2 nm Au NPs as a benchmark system in which hydrogen chemisorption and surface restructuring can unlock catalytic behavior absent in bulk gold. [9-10].

For more than three decades, Au NPs reactivity has largely been rationalized within an "under-coordination paradigm", where corners, edges, and vertex sites act as the primary active motifs. This view has been strengthened by the success of coordination-based descriptors, such as the coordination number (CN) [11-12] and generalized coordination number (GCN) [13-14], and by scaling relationships linking adsorption energetics to local coordination environments across facets, steps, and terraces. While powerful for descriptor discovery and catalyst screening, these approaches implicitly assume a static lattice and a fixed adsorption sites. In this framework, surface structure is treated as a geometric input rather than as a dynamic variable that can be reshaped by the reactive environment [15-17]. This static picture is increasingly challenged by *in-situ* and operando observations showing that ultrasmall Au is intrinsically fluxional [18] and can undergo gas-driven structural transitions under working conditions [19-24]. Aberration-corrected environmental TEM under reactive gases (including H_2 [19] and CO [20]) has revealed size-dependent restructuring on supported Au, up to partial loss of fcc order below a few nanometers under hydrogen atmospheres. These findings are particularly consequential in the sub-2 nm regime, where multiple morphologies (e.g., Ico vs fcc-derived Wulff shapes such as TOh) are often close in energy [25-26] and therefore easily interconverted by adsorbate-induced forces. Collectively, they motivate a revised viewpoint in which dynamic morphology, not only static under-coordination, can govern the nature and population of active sites on ultrasmall Au.

Hydrogen is particularly disruptive because adsorption can simultaneously reshape NP geometry and redistribute electronic density [19, 23, 27-29]. In an early DFT study of H_2 dissociation on small Au clusters, Barrio et al. showed that activation can involve structural fluxionality, cooperative participation of several Au atoms, and ensemble effects, rather than a single rigid adsorption site [30]. Subsequent theoretical studies further established that the atomic and electronic structures, finite-temperature isomer populations, and catalytic properties of bare, ligand-protected, and supported Au clusters can depend on fluxional ensembles and on the surrounding reactive environment [31–35]. However, much of this literature has focused on clusters containing only a few to a few tens of Au atoms, generally under isolated-adsorbate or low-coverage conditions. The hydrogen-rich, near-monolayer regime on larger sub-2 nm Au nanoparticles therefore remains comparatively less explored.

In a recent work, we have reported that hydrogen adsorption on sub-2 nm Au can drive pronounced surface and subsurface reconstruction, including terrace disruption and the emergence of well-ordered 1-D chain-like Au–H–Au–H–Au motifs [19]. However, the chemical identity of hydrogen and gold on these motifs and the appropriate use of the term “hydride” remains actively debated [29, 36]. Similar uncertainty surrounds the extent to which hydrogenated surface sites in ultrasmall gold NPs should be regarded as metallic or non-metallic in character [37-38]. In molecular gold hydrides, the metal–hydrogen bonding is commonly described as covalent in character, with Au atoms (electronegativity 2.54 on the Pauling scale) bearing partial negative charge and hydrogen atoms (electronegativity 2.20) being partially positive [39]. Whether this polarity and bonding picture carries over to hydrogen bond at metallic gold interfaces under varied coverage, however, remains far from obvious [36]. Insight into this question was provided from the work of Nguyen et al., who, using X-ray diffraction (XRD) together with Raman spectroscopy and DFT/phonon analysis, reported an unusual lattice contraction in hydrogen-implanted gold thin films. This contraction was interpreted as evidence for dynamic gold–hydrogen interactions within an otherwise electronically delocalized lattice [29]. Curiously, and to the best of our knowledge, the theoretical literature on the restructures Au NPs of hundreds of atoms under hydrogen remains underdeveloped, and a detailed molecular description of surface electronic structure and hydrogen-driven dynamics has not been reported.

At catalytic interfaces, the debate is sharpened by spectroscopic ambiguity surrounding the formation and the nature of surface gold hydrides. Bands in the ~2125–2130 cm^{-1} region,

View Article Online
DOI: 10.1039/D6NR01396A

historically reported on Au/ceria and related supports under H_2, have been variably assigned either to support-related electronic features or to a chemically distinct Au–H stretching vibration associated with Au–H hydride species [40-41]. Comparative FTIR studies on Au supported on different oxides further reported additional bands around ~1600–1620 cm^{-1} (and, on ceria, also ~1800 cm^{-1}) and attributed them to Au–H stretching modes, consistent with hydrogen bound to under-coordinated Au and/or bridging Au–H–Au environments [41]. Overall, this uncertainty is not merely semantic: whether hydrogen is best described as weakly adsorbed H, as a localized Au–H fragment, or as a polarized, hydride-like Au–H–Au motif has direct implications for how hydrogenation pathways, charge transfer, and site stability are modeled.

Building on this evolving context, the present work provides a systematic DFT and *ab initio* molecular dynamics (AIMD) assessment of hydrogen-induced restructuring in two prototypical sub-2 nm morphologies, icosahedral Au_{147} and truncated-octahedral Au_{201}. These two morphologies were examined across three representative hydrogenation states: (I) fixed-lattice adsorption (Au frozen, H relaxed), (II) fully relaxed 0 K Au+H structures, and (III) thermally accessible configurations sampled by AIMD at 300 K and subsequently quenched. We quantify hydrogen-driven structural evolution using radial distribution functions and coordination analyses, and we decompose adsorption energetics into intrinsic Au–H interactions and metal-deformation contributions to isolate how reconstruction stabilizes hydrogenated surfaces. To address the hydride debate directly, we characterize hydrogen polarity and bonding via Bader charge analysis, electronic density of states, electron-localization function, non-covalent interactions index, frontier reactivity, and vibrational fingerprints. The persistence of a delocalized, metal-like electronic network under near-monolayer hydrogen coverage indicates that the reconstructed surface is not electronically passivated; instead, it remains capable of supporting charge redistribution and H-transfer events, consistent with catalytic performances under hydrogenation conditions. Finally, we link the hydrogen-restructured active state to function by revisiting ethene hydrogenation on well-ordered chain motifs and contrasting the resulting mechanism with the historical static-lattice paradigm. Overall, our results position hydrogen not only as a reactant but also as a structure-directing agent that reshapes the active ensemble in ultrasmall Au, with direct consequences for activity and selectivity.

View Article Online
DOI: 10.1039/D6NR01396A

II. Results and Discussion

Hydrogen adsorption on sub-2 nm Au NPs is not a passive coverage effect but a coupled structural–electronic response that reshapes the active surface. In this section, we first establish that near-monolayer hydrogen drives a contracted Au–H–Au chain network on both icosahedral and truncated-octahedral morphologies. We then identify the electronic nature of this reconstructed state as polarized $Au^{\delta+}/H^{\delta-}$ bridging species embedded in a delocalized metallic network, before connecting these motifs to catalytic consequences in ethene hydrogenation and to vibrational fingerprints accessible to operando spectroscopy.

II.1. Hydrogen directs surface reconstruction into Au–H–Au chain networks

II.1.1. Chain formation under relaxation and at 300 K

We compare two sub-2 nm Au NP morphologies (Au_{147} Ico and Au_{201} TOh) under three hydrogenation states (see details in computational section and Supplementary Information). As reported in Figure 1, allowing the Au framework to relax (from Model I to Model II) triggers a qualitative change: hydrogen redistributes from hollow sites toward bridge and on-top environments while the outer Au layer reorganizes to form short Au–H–Au motifs. This reconstruction is particularly pronounced on Au_{147}, where the surface becomes largely disordered, while Au_{201} retains remnants of its original facets albeit strongly distorted (Fig. 1.a). Thermal sampling (Model III) at 300 K further orders this reconstructed shell into longer, better-defined Au–H–Au–H chain frameworks. In parallel, limited H_2 recombination/desorption occurs (6 H atoms for Au_{201} and 12 for Au_{147}), yielding $Au_{201}H_{116}$ and $Au_{147}H_{80}$. Importantly, the resulting surface is not “dehydrogenated”; rather, it stabilizes an extended, chain-rich hydrogenated state in which bridging H dominates, with a minor population of on-top H at terminal/apical chain positions. These results show that hydrogen does not merely populate pre-existing undercoordinated sites but rather, it actively rebuilds the surface into chain-like Au–H–Au networks. It is also important to emphasize that the present study focuses on the hydrogen-rich regime, in which hydrogen-induced restructuring is expected to be most pronounced. At sub-monolayer coverage, Au–H–Au motifs are not expected to be intrinsically excluded, but their formation should be progressive and local. Short chain-like fragments are likely to nucleate first in locally H-rich regions around highly under-coordinated edge and vertex sites, before extending toward more compact regions such as (100)

View Article Online
DOI: 10.1039/D6NR01396A

and (111)-type facets as the local hydrogen coverage increases. Thus, isolated Au–H–Au motifs may already be accessible below one monolayer, whereas the extended Au–H–Au chain network discussed here corresponds to the hydrogen-rich limit. A quantitative determination of the critical coverage for chain nucleation requires systematic finite-temperature sampling over many hydrogen coverages, nanoparticle sizes, and morphologies. This question is being addressed in a dedicated study using a DFT-trained machine-learning interatomic potential.

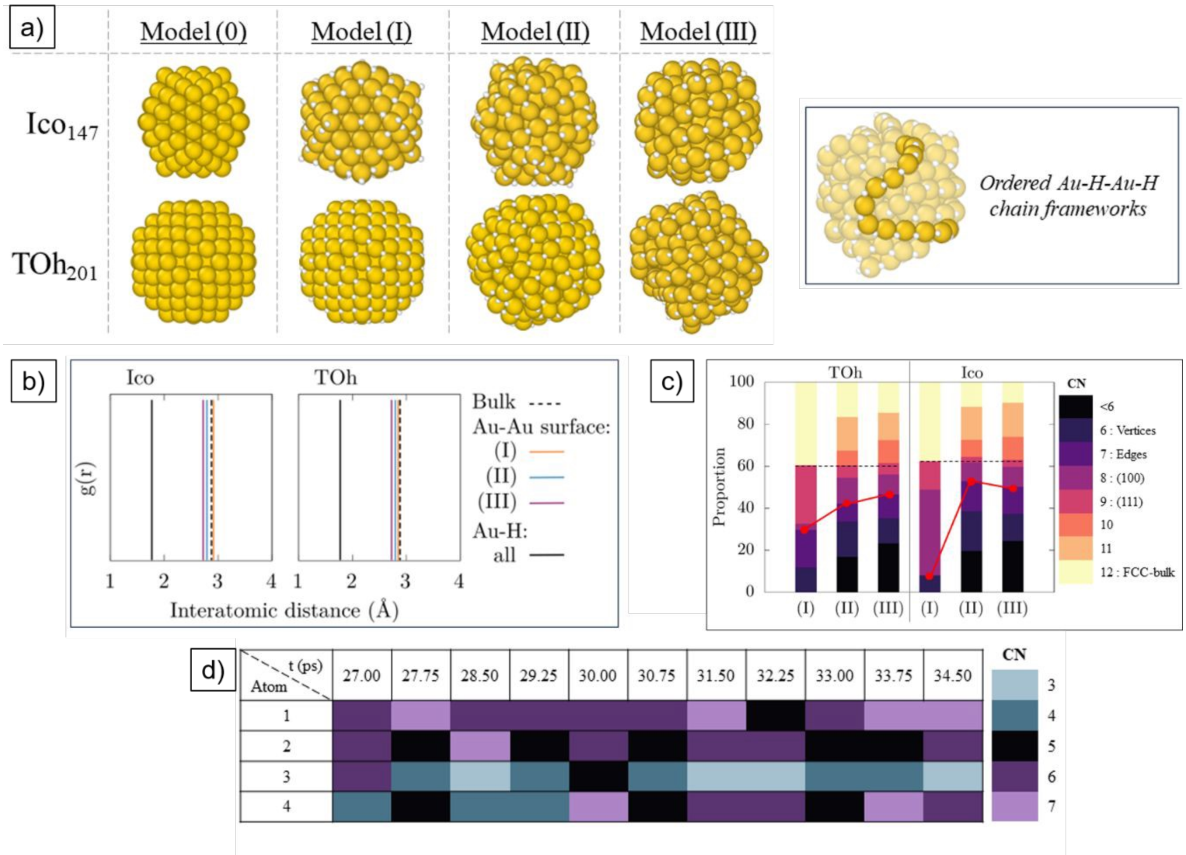

Figure 1: ***Hydrogen-driven surface reconstruction and dynamic low-coordination Au ensembles in sub-2 nm gold NPs.*** *(a) Representative structures of Ico Au$_{147}$ (top row) and TOh Au$_{201}$ (bottom row) for Model 0 (pristine nanoparticle), Model I (fixed-lattice adsorption: Au atoms frozen and H atoms relaxed), Model II (fully relaxed Au+H structure at 0 K), and Model III (representative structure sampled by AIMD at 300 K and subsequently quenched), showing the progressive reorganization of the outer shell under hydrogen coverage. Inset: Close-up of a representative Model III region highlighting the formation of ordered Au–H–Au–H chain frameworks. (b) Summary of first-neighbor distances extracted from surface-restricted radial distribution functions for Ico and TOh NPs. Colored markers denote the surface Au–Au first-neighbor peak positions for Models I–III, the black marker denotes the Au–H first-shell distance, and the dashed line indicates the bulk Au–Au nearest-neighbor distance. (c) Distribution of surface Au atoms by coordination number (CN; Au–Au cutoff = 3.5 Å) for Models I–III in TOh and Ico NP; the red line gives the cumulative fraction of low-coordination surface atoms (CN ≤ 7) and the dashed horizontal line marks the fraction of surface atoms in the NP. (d) Time evolution of the CN of four representative surface Au atoms belonging to an Au–H–Au chain in TOh during AIMD at 300 K, illustrating reversible coordination fluctuations and fluxional bond exchange within the reconstructed hydrogen-bridged surface. Yellow and white spheres represent Au and H atoms, respectively.*

View Article Online
DOI: 10.1039/D6NR01396A

II.1.2. Quantifying surface compaction and loss of medium-range order

To quantify the reconstruction of this hydrogen-rich regime, we analyze surface-restricted radial distribution functions (RDFs) for Au–Au and Au–H pairs (Fig. 1.b). Complete RDF profiles including core-restricted analyses are provided in the Supporting Information (Figs SI.1 and SI.2). In Model I, the surface Au–Au first-neighbor peak lies near the bulk value, reflecting the initial lattice order of each morphology. Upon relaxation under hydrogen (Model II), the surface Au–Au peak collapses to shorter distances in both NPs, consistent with hydrogen-bridged motifs pulling near-surface Au atoms together. After AIMD sampling (Model III), surface compaction is further reinforced, with the first-neighbor peak shifting to even shorter distances in both morphologies, indicating that thermal accessibility enhances the stability of contracted Au–Au contacts within the hydrogenated shell.

Concurrently, the surface Au–H first-shell peak remains centered near ~1.77 Å across models and morphologies (Fig. SI.1), but it narrows from Model I to Model III, consistent with a progressively more uniform H environment dominated by bridging geometries along the chain network. A minority of terminal/apical H species exhibits shorter Au–H distances, reflecting residual heterogeneity at chain ends and local junctions. Beyond the first peak, hydrogen adsorption strongly attenuates medium-range order in the surface RDFs, consistent with terrace disruption and chain formation. Overall, the surface-restricted RDFs show that hydrogen compacts near-surface Au–Au bonds while preserving a nearly invariant Au–H first-shell distance, thereby stabilizing a contracted, chain-rich active surface ensemble. Consistently, the core-restricted RDFs (Fig. SI.2) indicate that restructuring remains primarily surface-localized, with the NP interior displaying only a secondary strain redistribution (partial recovery toward fcc-like packing in TOh, while Ico retains residual internal strain) transmitted from the reconstructed shell.

II.1.3. Dynamic generation of low-coordination surface atoms

Coordination-number (CN) analysis provides a complementary picture of reconstruction (Fig. 1.c and Fig. SI.3a). Relative to the rigid-lattice reference, relaxation under hydrogen converts a significant fraction of terrace-like surface atoms (CN ≈ 8–9) into low-coordination atoms (CN ≤ 7). Notably, the chain ensemble introduces CN < 6 environments that are absent from the static lattice description and cannot be described as simple "edges" or "vertices" of the pristine morphology. In Model III, despite partial H_2 desorption, the population of $CN \leq 7$ remains high, demonstrating that hydrogen not only creates low-coordination sites but also dynamically maintains them at 300 K.

AIMD further reveals reversible CN fluctuations for Au atoms involved in Au–H–Au chains (Fig. 1.d; see also Fig. SI.3b and Movie M1), evidencing fluxional interconversion among local motifs and continuous Au–Au bond exchange with near-subsurface neighbors while preserving a hydrogen-bridged framework. Thus, undercoordination is not a transient defect but a dynamically sustained property of the chain network at 300 K. Because edge-like and chain-like environments can display similar Au–Au CN values, CN alone does not uniquely define the reactive motif; rather, the relevant “site identity” emerges from the connected Au–H–Au framework, which naturally enables concerted rearrangements of local geometry and, potentially, energetic and electronic distribution along the chain. This motivates the electronic analysis developed in the next sub-section.

II.2. Electronic identity of the chain state: polarized H in a delocalized metallic network

II.2.1. Energetic driving forces: Au–H stabilization versus metal deformation

Energetic decompositions with detailed values depicted in Table SI.1 show that, although pristine Au_{201} (TOh) is slightly more stable than Au_{147} (Ico), both morphologies exhibit the same energetic response to hydrogenation. Allowing the Au framework to relax under near-monolayer H coverage stabilizes the intrinsic Au–H interaction by ≈ 0.43 eV per H from Model I to Model III, whereas the associated metal-deformation penalty remains modest when expressed per Au atom (≈ 0.11–0.160 eV per Au). Because these two contributions oppose each other, the net adsorption energy becomes only ≈ 0.15–0.180 eV per H more exothermic across Models I–III. This near-cancellation indicates that hydrogen-driven reconstruction is energetically accessible and is primarily promoted by the stabilization of bridging Au–H–Au environments in the reconstructed shell.

II.2.2. Bader charge analysis and heterogeneity along Au–H–Au chains

Bader charge analysis establishes a robust polarity of the reconstructed state (Fig. 2.a). Even in the rigid-lattice reference, hydrogen adsorption induces $Au^{\delta+}/H^{\delta-}$ polarization. This polarity becomes markedly enhanced once reconstruction occurs and is most pronounced along chain frameworks in Model III, where positive charge accumulates on surface Au atoms while bonded hydrogen becomes increasingly negative. In contrast, the core of the NP remains close to neutral

View Article Online
DOI: 10.1039/D6NR01396A

on average, indicating that the electronic perturbation is primarily localized within the reconstructed shell.

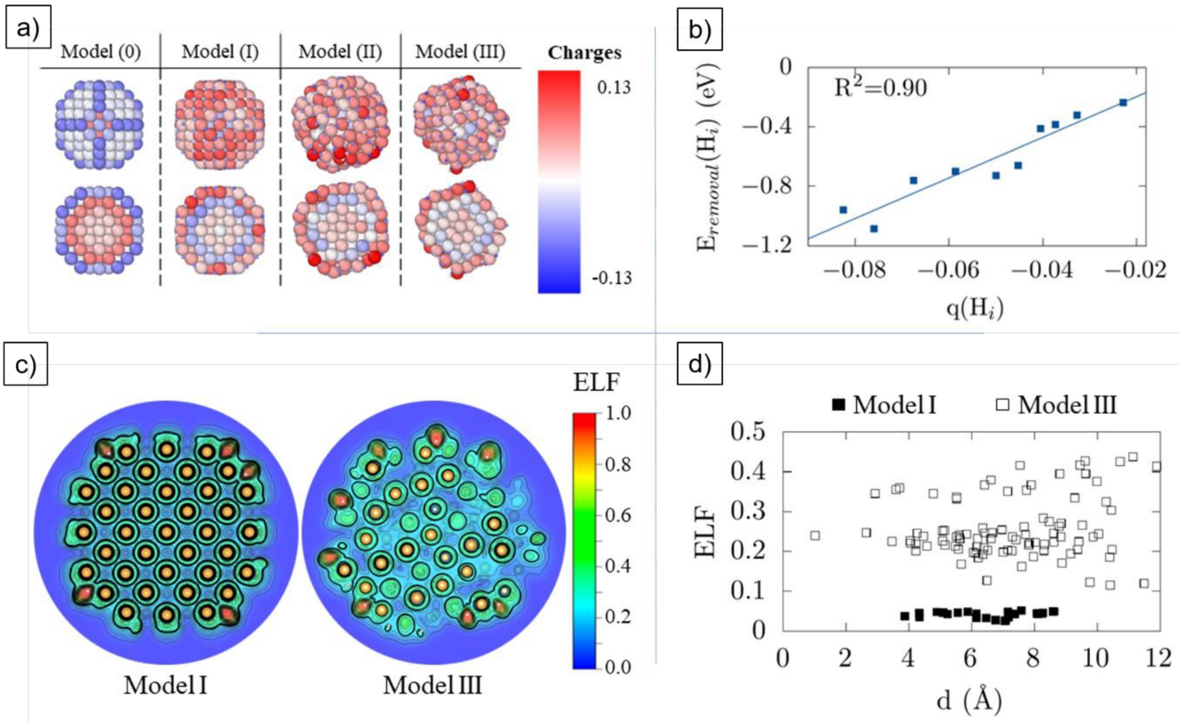

Figure 2: ***Electronic identity of the hydrogen-reconstructed Au–H–Au chain state.*** *(a) Bader-charge maps for the representative hydrogenated Au NP, shown as external views (top row) and cross-sectional views (bottom row) for Model 0 (pristine nanoparticle), Model I (fixed-lattice adsorption), Model II (fully relaxed Au+H structure at 0 K), and Model III (AIMD-derived structure sampled at 300 K and subsequently quenched). Upon hydrogen adsorption and reconstruction, positive charge progressively develops on outer-shell Au atoms, whereas bonded H atoms become negatively charged, evidencing a polarized* $Au^{\delta+}/H^{\delta-}$ *surface state mainly localized in the reconstructed shell. (b) Correlation between the Bader charge* $q(H_i)$ *of individual hydrogen atoms and their corresponding removal energies* $E_{removal}(H_i)$ *in Model III. More negatively charged H species are more strongly bound to the Au surface, highlighting the chemical heterogeneity of hydrogen within the chain network. The solid line is a linear fit. (c) Mid-plane ELF cross-sections for Model I and Model III shown as filled contours. Reconstruction transforms the outer shell into a more heterogeneous but still electronically connected network; no localized molecular AuH-like fragment is identified, consistent with Au–H–Au motifs embedded in a delocalized metallic scaffold. (d) Au–Au ELF saddle-point values extracted from the ELF topological network as a function of radial distance d from the NP center. Relative to Model I, Model III exhibits higher and broader outer-shell ELF values, evidencing redistribution of metallic connectivity within the reconstructed near-surface region. Together, the Bader and ELF analyses support a picture of hydride-like* $Au^{\delta+}/H^{\delta-}$ *polarity embedded in a delocalized metallic framework.*

Importantly, surface hydrogen is electronically heterogeneous, and this heterogeneity is chemically meaningful. Removing individual H atoms from the Model III structure reveals that more negatively charged H species bind more strongly (Fig. 2b), with variations in removal energies spanning ~1 eV across the sampled charge window. This correlation links the “hydride-like” character directly to site stability within the chain network.

View Article Online
DOI: 10.1039/D6NR01396A

II.2.3. ELF topology and charge redistribution: hydride-like polarity without localized Au–H bonds

The $Au^{\delta+}/H^{\delta-}$ polarity evidenced by Bader analysis does not, by itself, distinguish between localized, molecular-like Au–H fragments or a collective polarization of a metallic surface. We therefore combine real-space descriptors that probe electron localization/connectivity (ELF topology and charge-density differences $\Delta\rho$) with energy-resolved and response descriptors (TDOS/PDOS and Fukui functions) to assess whether the reconstructed shell behaves as a molecular hydride phase or as a polarized metallic network.

In the ELF framework, most two-center covalent bonds are associated with a disynaptic valence basin [42-43]. However, this is not the case of hydrogen which only has one electron. To gain insight into the interactions, the ELF can instead be analyzed at the saddle points between Au and H. As a first indication, the isosurfaces clearly show that the Au–H–Au bridges are not isolated AuH-like fragments, but rather delocalized interactions embedded in the metallic scaffold (Fig. 2.c). Comparison of the saddle-point ELF values across the different models further shows that reconstruction reshapes metallic cohesion within the outer shell. The distribution of Au–Au ELF saddle-point values connecting neighboring Au basins shifts upward and broadens toward the surface in Model III (Fig. 2.d). This systematic evolution indicates that surface reconstruction does not disrupt Au–Au connectivity; rather, it redistributes it (see Fig. SI.4). The outer shell therefore adopts a contracted yet electronically connected near-surface Au network, in which bonding interactions become more heterogeneous but remain topologically continuous. This interpretation is reinforced by complementary real-space descriptors. Non-covalent interaction (NCI) analysis, which highlights weak density-overlap regions such as dispersive contacts, shows that interactions between adjacent chain segments are predominantly weak and van der Waals–like (Fig. SI.5). Accordingly, the reconstructed shell is not stabilized by strong lateral Au–Au bonds between chains, but instead behaves as a fluxional ensemble primarily held together by the polarized Au–H–Au framework. The ELF and NCI analyses thus converge toward a picture of electronically connected chains with weak inter-chain cohesion.

Charge-density differences ($\Delta\rho$) provide the electronic origin of this behavior. Electron accumulation occurs on H, while depletion develops in the outer Au layer, with a depletion component extending into Au–Au regions of the reconstructed shell (Fig. SI.6). This Au→H charge transfer competes directly with lateral Au–Au bonding, thereby softening and

DOI: 10.1039/D6NR01396A

reorganizing the surface metallic network. Reconstruction is therefore not merely geometric but electronically driven, as polarization toward hydrogen destabilizes conventional surface Au–Au interactions and promotes the emergence of contracted Au–H–Au chains. Despite this polarity and structural reorganization, the energy-resolved electronic structure demonstrates that the NP retains a clear metallic character under near-monolayer hydrogen coverage. The pristine clusters exhibit sharp, highly structured TDOS features characteristic of finite-size quantization and high symmetry, whereas H adsorption (with or without reconstruction) smooths and broadens the spectrum, reflecting symmetry breaking and a wider distribution of local Au environments (Fig. SI.7). In all hydrogenated models, the TDOS remains finite at E_F and the near-E_F states are dominated by delocalized Au 6s/6p character, ruling out electronic passivation or "molecularization" into AuH-like units (Figs. SI.7–SI.9). Hydrogen instead introduces a robust deep-valence feature around ~−8.5 eV assigned to Au(5d)–H(1s) hybridization (Fig. SI.8). Locally, reconstruction compresses and upshifts the Au 5d manifold, shifting the d-band center from $\varepsilon_d \approx -3.68$ eV at an edge site (Model I) to $\varepsilon_d \approx -3.29$ eV at a chain site (Model III), while the H-projected signal becomes more structured and redistributes toward higher energies, consistent with a more multicenter Au–H–Au interaction along the chain network (Fig. SI.8). Site-resolved PDOS further highlights enhanced heterogeneity upon relaxation without loss of metallic DOS at E_F (Fig. SI.9). Overall, DOS/PDOS analyses reconcile hydride-like polarity with a delocalized metallic backbone whose local d-states are reshaped by chain formation. Finally, Fukui-function maps extend this collective picture to frontier reactivity. In the fixed-lattice reference, donor and acceptor regions remain localized at vertices and edges, consistent with the classical undercoordination paradigm. Upon chain formation, however, the Fukui response spreads along the Au–H–Au network, indicating that reactivity is no longer confined to isolated hot spots but delocalized over an electronically cooperative chain ensemble (Fig. SI.10). Taken together, ELF topology, NCI analysis, charge redistribution, DOS signatures, and Fukui functions consistently describe a hydrogen-driven reconstruction that preserves a delocalized metallic backbone while introducing hydride-like polarity. The resulting $Au^{\delta+}/H^{\delta-}$ chain network is therefore electronically collective, structurally adaptive, and catalytically active rather than electronically quenched.

II.3. Catalytic consequences: chain sites attenuate the thermodynamic driving force for ethene hydrogenation

Supported Au NPs are widely recognized for their high selectivity in acetylene hydrogenation to ethene, exhibiting limited propensity for subsequent ethene hydrogenation under relevant feed conditions [44-45]. To assess how hydrogen-induced Au–H–Au chain reconstruction influences this selectivity, we compare stepwise C_2H_4 hydrogenation on Model I and Model III of TOh NP, where near-monolayer hydrogen coverage stabilizes bridging motifs.

Although ethene can in principle, bind through π adsorption on a single Au atom or via di-σ coordination bridging two Au atoms [46-47], the scarcity of accessible atop sites on the chain-saturated surface and the structural cost associated with disrupting multiple bridges render di-σ binding the most compatible mode with the reconstructed state. Accordingly, for Model III, adsorption is generated by removing one bridging H from a representative chain arrangement followed by local relaxation of the surrounding Au/H environment (more details are provided in the Supporting Information and in Fig. SI.11). The resulting reaction-free energy profiles reported in Figure 3 show that, despite the dense hydrogenated shell, di-σ adsorption remains accessible and is even slightly less endothermic on the chain site (+0.205 eV) than on the representative edge site of Model I (+0.385 eV). This result indicates that reconstruction does not penalize initial C_2H_4 binding. The decisive contrast instead emerges in hydrogen-transfer thermodynamics. On the rigid edge site, the first H-addition is favorable, with $C_2H_5^*$ lying 0.215 eV below $C_2H_4^*$ ($\Delta G_1 = -0.215$ eV), whereas on the chain site this step becomes endergonic, placing $C_2H_5^*$ 0.318 eV above $C_2H_4^*$ ($\Delta G_1 = +0.318$ eV); similarly, the second H-addition is markedly less exergonic on the chain ensemble ($\Delta G_2 = -0.696$ eV) than on the edge (−1.262 eV). Thus, while adsorption energetics remain comparable within a few tenths of an eV, chain motifs substantially attenuate the thermodynamic driving force toward ethane formation. This moderation originates from the collective nature of the reconstructed shell. As the transferring hydrogen is part of a polarized Au–H–Au bridge that concurrently stabilizes the contracted near-surface Au framework, so hydrogen transfet to C_2H_4 entails an energetic penalty associated with reorganizing these linkages. The chain ensemble therefore behaves as a self-stabilized hydrogen reservoir that accommodates unsaturated adsorbates while reducing the thermodynamic driving force for excessive hydrogen transfer. In this way, hydrogen-directed reconstruction simultaneously preserves adsorption accessibility and attenuates the propensity toward ethene over-hydrogenation, providing a thermodynamic rationale for the high selectivity characteristic of ultrasmall Au catalysts under hydrogenation conditions. We note however, that a full kinetic treatment including all possible adsorption motifs and transition states would require a dedicated study beyond the scope of the present work.

View Article Online
DOI: 10.1039/D6NR01396A

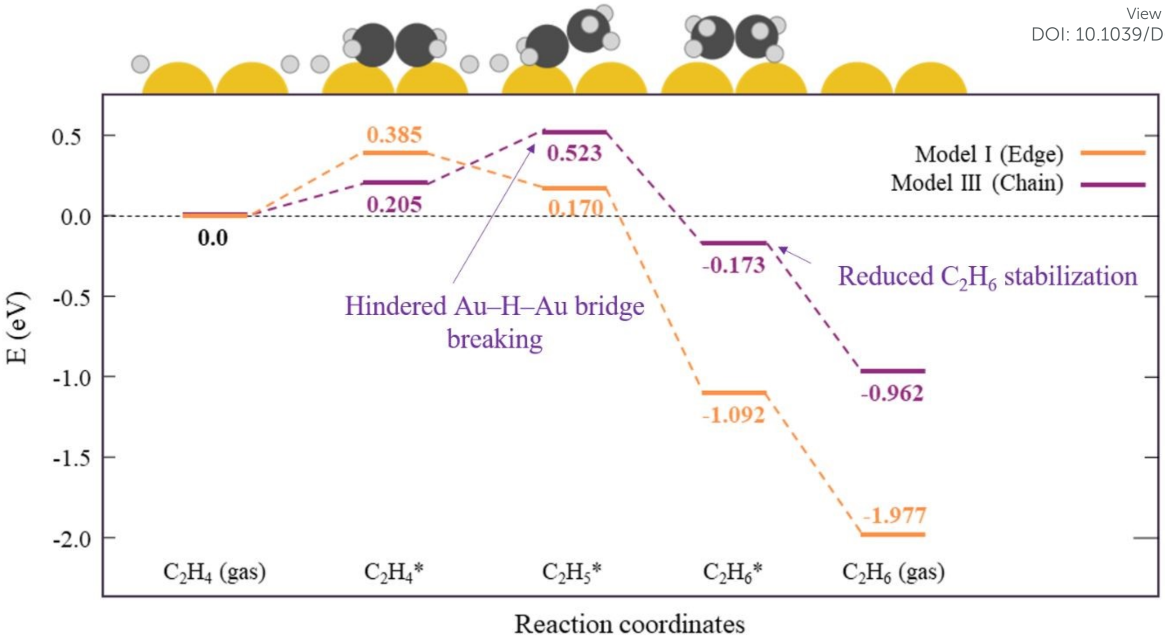

Figure 3: ***Reaction-energy diagram for stepwise ethene hydrogenation on rigid-lattice edge site (Model I) and on AIMD-derived Au–H–Au chain site (Model III).*** *Relative Gibbs free energies at 300 K* ($\Delta G_{300\,K}$, *eV) are reported for optimized intermediates and referenced to* $C_2H_4(g)$ *+ the corresponding pre-prepared H-covered surface (0.0 eV; see Supporting Information for site preparation/constraints and table SI.2 for energy references). Ethene binds in a di-σ configuration* (C_2H_4*), *followed by optimized minima for the ethyl* (C_2H_5*) *and ethane* (C_2H_6*) *surface intermediates; the final state corresponds to* $C_2H_6(g)$ *after desorption. Connecting lines are guides to the eye.*

II.4. Vibrational fingerprints of Au–H motifs for operando identification

Finally, to connect the reconstructed Au–H–Au network with operando spectroscopy, we computed harmonic vibrational modes for representative AIMD-derived structures (Model III). The Au–H stretching region splits into distinct motif-dependent families (Figure 4). Terminal/apical Au–H species (Au–H ≈ 1.58–1.60 Å) yield high-frequency stretches in the ~2000–2160 cm^{-1} range (see table SI.3), overlapping the debated ~2125–2130 cm^{-1} window often reported on the literature for supported Au/CeO_2 [48-49], (more data and literature details are provided in Supplementary Information, Table SI.3). Bridging H within Au–H–Au chain motifs (Au–H ≈ 1.69–1.77 Å) gives lower-frequency bands around ~1630–1680 cm^{-1}, consistent with the ~1620 cm^{-1} features assigned to Au–H on several oxide supports. More constrained chain-intersection environments produce intermediate frequencies (~1785 cm^{-1}), close to the ~1800 cm^{-1} band reported on Au/CeO_2. These assignments rationalize the coexistence of multiple Au–H-related bands (terminal/apical vs bridging in Au–H–Au chains vs more constrained chain-intersection environments), rather than a single “universal” Au–H frequency.

View Article Online
DOI: 10.1039/D6NR01396A

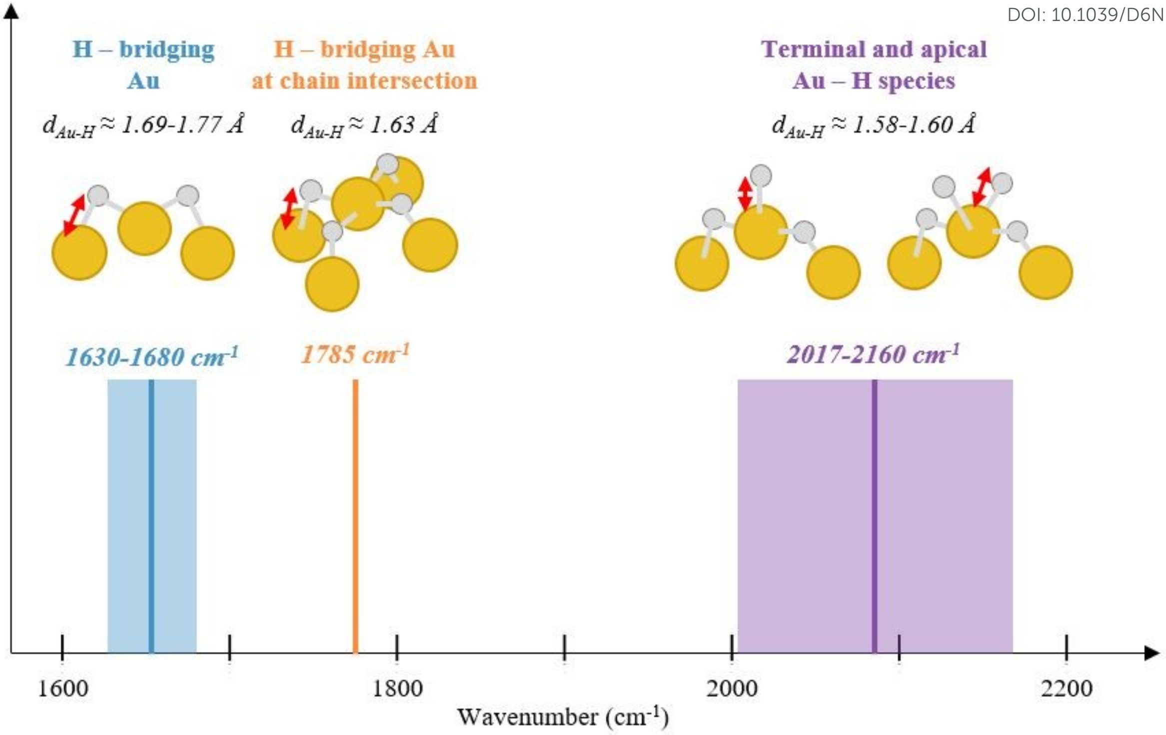

Figure 4: ***Vibrational fingerprints of Au–H motifs derived from AIMD (Model III) for operando identification:*** *Computed harmonic Au–H stretching frequencies are resolved into motif-dependent families. Bridging hydrogen in Au–H–Au chain configurations ($d_{Au\text{–}H} \approx 1.69\text{–}1.77$ Å) gives rise to low-frequency bands at 1630–1680 cm^{-1}. More constrained environments at chain intersections yield intermediate frequencies around 1785 cm^{-1} ($d_{Au\text{–}H} \approx 1.63$ Å). Terminal and apical Au–H species ($d_{Au\text{–}H} \approx 1.58\text{–}1.60$ Å) produce high-frequency modes in the 2017–2160 cm^{-1} range. These assignments rationalize the coexistence of multiple Au–H spectral features reported experimentally, rather than a single characteristic Au–H stretching frequency.*

III. Conclusion

Hydrogen adsorption on sub-2 nm Au NPs induces a coupled structural–electronic transformation that redefines the catalytic ensemble. Across both icosahedral Au_{147} and truncated-octahedral Au_{201} morphologies, near-monolayer hydrogen coverage reconstructs the outer shell into a contracted Au–H–Au chain network and dynamically sustains a high population of fluxional low-coordination surface atoms at 300 K. Charge partitioning demonstrates systematic Au→H electron transfer, yielding polarized $Au^{\delta+}/H^{\delta-}$ bridging species whose site-dependent stability is chemically significant. Real-space electronic descriptors (ELF topology and charge-density differences) indicate that this hydride-like polarity does not correspond to localized molecular Au–H bonding; instead, the reconstructed shell remains

View Article Online
DOI: 10.1039/D6NR01396A

embedded in a delocalized metallic network reorganized by collective surface polarization. These structural and electronic fingerprints translate into catalytic consequences. In ethene hydrogenation, chain motifs provide accessible di-σ adsorption environments while intrinsically moderating hydrogen-transfer energetics because key steps disrupt stabilizing Au–H–Au bridges, thereby preventing facile over-hydrogenation to ethane. Moreover, normal-mode analysis predicts three diagnostic Au–H stretching families, providing operando-testable IR fingerprints for identifying the chain ensemble. Together, these findings establish Au–H–Au chain networks as the hydrogen-stabilized active ensemble on ultrasmall gold NPs and provide a mechanistic explanation for their outstanding performance and selectivity under hydrogenation conditions. More broadly, this work suggests that the chemistry of ultrasmall gold under reactive atmospheres should be understood not through static site descriptors alone, but as an adsorbate-shaped, dynamically polarized metallic ensemble. This perspective raises the question of whether other gases can similarly imprint distinct structural–electronic states, opening new routes to understand and control reactivity and selectivity on sub-2 nm Au.

IV. Computational details

Model construction: To elucidate how hydrogen reshapes the structure and electronic properties of ultrasmall Au NPs, we performed a systematic model study combining density functional theory and *ab initio* molecular dynamics. Two representative sub-2 nm morphologies of Au NPs comprising a few hundred atoms were considered: a truncated-octahedral (TOh) NP with 201 atoms (1.69 nm) and an icosahedral (Ico) NP with 147 atoms (1.52 nm). The TOh morphology was generated via Wulff construction using DFT-calculated surface energies $\gamma_{100} = 0.11$ eV.Å^{-2} and $\gamma_{111} = 0.09$ eV.Å^{-2} [50]. Both NPs were considered under full hydrogen coverage ($\theta = 1$ ML), corresponding to 122 and 92 surface adsorbed H atoms for TOh and Ico, respectively, i.e., one H atom per surface atom. This coverage was selected to probe the hydrogen-rich limit, where adsorbate-induced restructuring is expected to be maximized.

For each morphology, we compared four models (Fig. 1). The first is pristine reference denoted Model 0 which corresponds to H-free TOh and Ico NPs. Model I referred to as “Fixed-lattice adsorption”, considers Au atoms frozen in the positions of the pristine NP, while adsorbed hydrogen atoms are fully relaxed. In this model, H atoms are positioned on high-symmetry sites, consistent with the literature, namely 3-fold sites on compact (111) facets and bridge sites on (100) facets and edge sites [51]. This setup isolates purely electronic effects of hydrogen at

View Article Online
DOI: 10.1039/D6NR01396A

constant Au geometry. Model II referred to as "Fully relaxed at 0 K" allows the entire NP+H system to relax within DFT optimization in order to quantify static, H-induced reconstructions. Model III, referred to as "AIMD at 300 K", is based on representative structures extracted from AIMD simulations at 300 K and subsequently refined by 0 K relaxation. This last model captures thermally assisted restructuring of core and surface NPs as well as partial hydrogen desorption.

Electronic-structure calculations:

Spin-unpolarized DFT calculations were performed using VASP package [52] within the projector augmented wave (PAW) [53-54] formalism and the Perdew–Burke–Ernzerhof (PBE) generalized-gradient approximation for exchange-correlation [55]. To account for van der Waals interactions, Grimme's D3 dispersion corrections were considered [56]. The plane-wave kinetic-energy cutoff was set to 500 eV and Brillouin-zone sampling was restricted to the Γ point. Electronic self-consistency and ionic relaxations employed thresholds of EDIFF = 10^{-6} eV and EDIFFG = −0.01 eV.$Å^{-1}$, respectively. AIMD simulations were carried out in the canonical ensemble (NVT) at 300 K using a Nosé–Hoover thermostat [57-58] and a time step of 1.5 fs. To improve numerical stability for hydrogen-containing trajectories, hydrogen mass scaling was applied by setting POMASS = 3 in VASP. No additional geometric constraints were used during AIMD. This mass scaling affects only the nuclear dynamics and the effective sampling time scale, while leaving the underlying Born–Oppenheimer potential energy surface and the quenched optimized structures unchanged. Trajectories up to 35 ps were used to generate Model III structures by sampling thermally equilibrated snapshots before final minimization at 0 K.

Structural, energetic and electronic analyses:

Hydrogen-induced structural reconstruction was quantified using radial distribution functions (RDFs) for Au–Au pairs, together with coordination numbers defined using a nearest-neighbor cutoff of 3.5 Å. These metrics were used to characterize changes in local order, undercoordination, and motif formation upon hydrogen adsorption. Adsorption energetics were analyzed through a decomposition scheme separating intrinsic Au–H interaction energies from the energetic penalty associated with NP deformation, allowing the stabilizing role of hydrogen-driven reconstruction to be isolated and compared across morphologies. Electronic structure and bonding were examined using total and projected densities of states, d-band center analysis, and spatially resolved charge redistribution descriptors, including charge-density difference maps. Hydrogen polarity and Au–H bonding character were quantified using Bader charge analysis [59] and complementary real-space analysis using the electron localization function (ELF) was employed to assess the Au-Au and Au–H interactions [42-43]. Vibrational properties were further characterized by normal-mode analysis to identify infrared-active stretching fingerprints associated with different types of adsorbed hydrogen. Finally, frontier reactivity was evaluated using Fukui-function–based descriptors to identify electron-donating and electron-accepting regions and to rationalize hydrogen activation and transfer events. Full methodological details, including all energetic definitions, equations, and electronic-structure descriptors, are provided in the Supporting Information.

CONFLICTS OF INTEREST

There are no conflicts of interest to declare

ACKNOWLEDGMENT

This work was granted access to the HPC resources of CCRT, CINES, and IDRIS under GENCI allocations A0170807369 and A0160915069. L. C. and N. F. B. acknowledge financial support from ED Chimie Balard and ED388, respectively, through doctoral fellowships. The authors are grateful to Jean-Sébastien Filhol for insightful discussions regarding the manuscript results and the Fukui analysis.

REFERENCES

[1] Masatake Haruta et al. “Novel Gold Catalysts for the Oxidation of Carbon Monoxide at a Temperature far Below 0°C”. In: Chem. Lett. 16.2 (Feb. 1987), pp. 405–408. issn: 0366-7022. doi: 10.1246/cl.1987.405.

[2] M. Haruta et al. “Gold catalysts prepared by coprecipitation for low-temperature oxidation of hydrogen and of carbon monoxide”. In: J. Catal. 115.2 (Feb. 1989), pp. 301–309. issn: 0021-9517. doi: 10.1016/0021-9517(89)90034-1.

[3] Masatake Haruta. “Size- and support-dependency in the catalysis of gold”. In: Catal. Today 36.1 (Apr. 1997), pp. 153–166. issn: 0920-5861. doi: 10.1016/S0920-5861(96)00208-8.

[4] A. Stephen K. Hashmi and Graham J. Hutchings. “Gold Catalysis”. In: Angew. Chem. Int. Ed. 45.47 (Dec. 2006), pp. 7896–7936. issn: 1433-7851. doi: 10.1002/anie.200602454.

[5] Xiao Yan Liu et al. “Catalysis by gold: New insights in to the support effect”. In: Nano Today 8.4 (Aug. 2013), pp. 403–416. issn: 1748-0132. doi: 10.1016/j.nantod.2013.07.005.

[6] Tamao Ishida et al. “Importance of Size and Contact Structure of Gold Nanoparticles for the Genesis of Unique Catalytic Processes”. In: Chem. Rev. 120.2 (Jan.2020), pp. 464–525. issn: 0009-2665. doi: 10.1021/acs.chemrev.9b00551.

[7] Hengwei Wang and Junling Lu. “A Review on Particle Size Effect in Metal-Catalyzed Heterogeneous Reactions”. In: Chin. J. Chem. 38.11 (Nov. 2020), pp. 1422–1444. issn: 1001-604X. doi: 10.1002/cjoc.202000205.

[8] Geoffrey C. Bond et al. “Hydrogenation over supported gold catalysts”. In: J. Chem. Soc., Chem. Commun. 13 (Jan. 1973), 444b–445. issn: 0022-4936. doi: 10.1039/C3973000444B.

[9] Markus M. Schubert et al. “CO Oxidation over Sup-ported Gold Catalysts - “Inert” and “Active” Support Materials and Their Role for the Oxygen Supply during Reaction”. In: J. Catal. 197.1 (Jan. 2001), pp. 113–122.issn: 0021-9517. doi: 10.1006/jcat.2000.3069.

[10] Raquel Juárez et al. “Heterolytic and heterotopic dis-sociation of hydrogen on ceria-supported gold nanoparticles. Combined inelastic neutron scattering and FT-IR spectroscopic study on the nature and reactivity of surface hydrogen species”. In: Chem. Sci. 1.6 (Nov.2010), pp. 731–738. issn: 2041-6520. doi: 10.1039/C0SC00336K.

[11] Giannis Mpourmpakis, Antonis N. Andriotis, and Dionisios G. Vlachos. “Identification of descriptors for the CO interaction with metal nanoparticles”. In: Nano Lett.10.3 (Mar. 2010), pp. 1041–1045. issn: 1530-6992. doi:10.1021/nl904299c. eprint: 20151700.

[12] Siwen Wang et al. “Coordination numbers for unraveling intrinsic size effects in gold-catalyzed CO oxidation”. In: Phys. Chem. Chem. Phys. 20.9 (Feb. 2018), pp. 6055–6059. issn: 1463-9076. doi: 10.1039/C8CP00102B.

[13] Federico Calle-Vallejo et al. “Finding optimal surface sites on heterogeneous catalysts by counting nearest neighbors”. In: Science 350.6257 (Oct. 2015), pp. 185–189. issn: 1095-9203. doi: 10.1126/science.aab3501.eprint: 26450207.

[14] Federico Calle-Vallejo et al. “Introducing structural sensitivity into adsorption energy scaling relations by means of coordination numbers”. In: Nat. Chem. 7.5 (May 2015), pp. 403–410. issn: 1755-4349. doi: 10.1038/nchem.2226. eprint: 25901818.

[15] F. Abild-Pedersen et al. “Scaling Properties of Adsorption Energies for Hydrogen-Containing Molecules on Transition-Metal Surfaces”. In: Phys. Rev. Lett. 99.1 (July 2007), p. 016105. doi: 10.1103/PhysRevLett.99.016105.

[16] J. K. Nørskov et al. “Towards the computational design of solid catalysts”. In: Nat. Chem. 1.1 (Apr. 2009), pp. 37–46. issn: 1755-4349. doi: 10.1038/nchem.121.eprint: 21378799.

[17] Franklin Feng Tao and Miquel Salmeron. “In situ studies of chemistry and structure of materials in reactive environments”. In: Science 331.6014 (Jan. 2011), pp. 171–174. issn: 1095-9203. doi: 10.1126/science.1197461.eprint: 21233377.

[18] Angelo Vargas et al. “Fluxionality of gold nanoparticles investigated by Born-Oppenheimer molecular dynamics”. In: Phys. Rev. B 80.19 (Nov. 2009), p. 195421.doi: 10.1103/PhysRevB.80.195421.

[19] Abdallah Nassereddine et al. “Revealing Size Dependent Structural Transitions in Supported Gold Nanoparticles in Hydrogen at Atmospheric Pressure”. In: Small 17.51 (Dec. 2021), p. 2104571. issn: 1613-6810. doi: 10.1002/smll.202104571.

[20] Yang He et al. “Size-dependent dynamic structures of supported gold nanoparticles in CO oxidation reaction condition”. In: Proc. Natl. Acad. Sci. U.S.A. 115.30 (July 2018), pp. 7700–7705. doi: 10.1073/pnas.1800262115.

[21] Adrian Chmielewski et al. “Reshaping Dynamics of Gold Nanoparticles under H2 and O2 at Atmospheric Pressure”. In: ACS Nano 13.2 (Feb. 2019), pp. 2024–2033. issn: 1936-0851. doi: 10.1021/acsnano.8b08530.

[22] Geng Sun and Philippe Sautet. “Metastable Structures in Cluster Catalysis from First-Principles: Structural Ensemble in Reaction Conditions and Metastability Triggered Reactivity”. In: J. Am. Chem. Soc. 140.8 (Feb. 2018), pp. 2812–2820. issn: 1520-5126. doi: 10.1021/jacs.7b11239. eprint: 29424224.

[23] Ryo Ishida et al. “Hydrogen-Mediated Electron Doping of Gold Clusters As Revealed by In Situ X-ray and UV–vis Absorption Spectroscopy”. In: J. Phys. Chem.Lett. 8.11 (June 2017), pp. 2368–2372. doi: 10.1021/acs.jpclett.7b00722.

View Article Online
DOI: 10.1039/D6NR01396A

[24] Abdelali Khelfa et al. “Selective shortening of gold nanorods: when surface functionalization dictates the reactivity of nanostructures”. In: Nanoscale 12.44 (Nov.2020), pp. 22658–22667. issn: 2040-3364. doi: 10.1039/D0NR06326F.

[25] Amanda S. Barnard et al. “Nanogold: A Quantitative Phase Map”. In: ACS Nano 3.6 (June 2009), pp. 1431–1436. issn: 1936-0851. doi: 10.1021/nn900220k

[26] Chen-Hui Chan et al. “Effect of the Ligand Binding Strength on the Morphology of Functionalized Gold Nanoparticles”. In: J. Phys. Chem. Lett. 11.7 (Apr.2020), pp. 2717–2723. issn: 1948-7185. doi: 10.1021/acs.jpclett.0c00300. eprint: 32146808.

[27] Dongxiao Chen and Philippe Sautet. “Atomistic Land-scape of Pt Nanoparticles via Machine Learning: How Size Effect and Hydrogen Adsorption Govern Structural Ensembles and Catalytic Activity”. In: Angew. Chem.138.2 (Jan. 2026), e19209. issn: 0044-8249. doi: 10.1002/ange.202519209

[28] William L. Watkins and Yves Borensztein. “Mechanism of hydrogen adsorption on gold nanoparticles and charge transfer probed by anisotropic surface plasmon resonance”. In: Phys. Chem. Chem. Phys. 19.40 (Oct.2017), pp. 27397–27405. issn: 1463-9076. doi: 10.1039/C7CP04843B.

[29] Khac Thuan Nguyen et al. “Unusual hydrogen im-planted gold with lattice contraction at increased hydrogen content”. In: Nat. Commun. 12.1560 (Mar. 2021), p. 1560. issn: 2041-1723. doi: 10.1038/s41467-021-21842-9.

[30] L. Barrio et al. “A density functional theory study of the dissociation of H2 on gold clusters: Importance of fluxionality and ensemble effects”. In: J. Chem. Phys. 125.16 (Oct. 2006), p. 164715. issn: 0021-9606. doi: 10.1063/1.2363971.

[31] Hannu Häkkinen. “Atomic and electronic structure of gold clusters: understanding flakes, cages and superatoms from simple concepts”. In: Chem. Soc. Rev. 37.9 (Sept. 2008), pp. 1847–1859. issn: 0306-0012. doi: 10.1039/B717686B.

[32] E. C. Beret et al. “Free gold clusters: beyond the static, monostructure description”. In: Faraday Discuss. 152 (July 2011), pp. 153–167. issn: 1359-6640. doi: 10.1039/C1FD00027F.

[33] M. Gao et al. “Application of Automated Reaction Path Search Methods to a Systematic Search of Single-Bond Activation Pathways Catalyzed by Small Metal Clusters: A Case Study on H–H Activation by Gold”. In: J. Chem. Theory Comput. 10.4 (Apr. 2014), pp. 1623–1630. issn: 1549-9618. doi: 10.1021/ct500068b.

[34] M. Gao et al. “Reactivity of Gold Clusters in the Regime of Structural Fluxionality”. In: J. Phys. Chem. C 119.20 (May 2015), pp. 11120–11130. issn: 1932-7447. doi: 10.1021/jp511913t.

[35] H. Zhai and A. N. Alexandrova. “Fluxionality of Catalytic Clusters: When It Matters and How to Address It”. In: ACS Catal. 7.3 (Mar. 2017), pp. 1905–1911. issn: 2155-5435. doi: 10.1021/acscatal.6b03243.

[36] I. P. Silverwood et al. “Evidence for a surface gold hydride on a nanostructured gold catalyst”. In: Chem.Commun. 52.3 (Dec. 2015), pp. 533–536. issn: 1359-7345. doi: 10.1039/C5CC06118K.

[37] Geoffrey and David. “Catalysis by Gold”. In: Catal.Rev. (Jan. 1999). issn: 1034-1523. url: https://www.tandfonline.com/doi/abs/10.1081/CR-100101171.

[38] Geoffrey C. Bond. “Hydrogenation by gold catalysts: an unexpected discovery and a current assessment”. In: Gold Bull. 49.3 (Dec. 2016), pp. 53–61. issn: 2190-7579.doi: 10.1007/s13404-016-0182-8.

[39] Xuefeng Wang and Lester Andrews. “Infrared Spec-tra and DFT Calculations for the Gold Hydrides AuH, (H2)AuH, and the AuH3 Transition State Stabilized in (H2)AuH3”. In: J. Phys. Chem. A 106.15 (Apr.2002), pp. 3744–3748. issn: 1089-5639. doi: 10.1021/jp014105f.

[40] Claude Binet, Ahmed Badri, and Jean-Claude Lavalley. “A Spectroscopic Characterization of the Reduction of Ceria from Electronic Transitions of Intrinsic Point Defects”. In: J. Phys. Chem. 98.25 (June 1994), pp. 6392–6398. issn: 0022-3654. doi: 10.1021/j100076a025.

[41] Maela Manzoli et al. “Hydrogen interaction with gold nanoparticles and clusters supported on different oxides: A FTIR study”. In: Catal. Today 181.1 (Feb. 2012), pp. 62–67. issn: 0920-5861. doi: 10.1016/j.cattod.2011.07.029.

[42] J. Contreras-Garcia and J. M. Recio. “Electron delocalization and bond formation under the ELF framework”. In: Theor. Chem. Acc. 128.4 (Mar. 2010), pp. 411–418.issn: 1432-881X. doi: 10.1007/s00214-010-0828-1.

[43] Erin R. Johnson et al. “Revealing Noncovalent Interactions”. In: J. Am. Chem. Soc. 132.18 (May 2010), pp. 6498–6506. issn: 0002-7863. doi: 10.1021/ja100936w.

[44] Jifei Jia et al. “Selective Hydrogenation of Acetylene over Au/Al2O3 Catalyst”. In: J. Phys. Chem. B 104.47 (Nov. 2000), pp. 11153–11156. issn: 1520-6106. doi: 10.1021/jp001213d.

[45] Andreea C. Gluhoi, Johan W. Bakker, and Bernard E. Nieuwenhuys. “Gold, still a surprising catalyst: Selective hydrogenation of acetylene to ethylene over Au nanoparticles”. In: Catal. Today 154.1 (Sept. 2010), pp. 13–20. issn: 0920-5861. doi: 10.1016/j.cattod.2010.02.021.

View Article Online
DOI: 10.1039/D6NR01396A

[46] C. F. Zinola and A. M. Castro Luna. “Adsorption configurations of ethylene and acetylene on gold”. In: J. Electroanal. Chem. 456.1 (Sept. 1998), pp. 37–46. issn:1572-6657. doi: 10.1016/S0022-0728(98)00210-1.

[47] Andrey Lyalin and Tetsuya Taketsugu. “Adsorption of Ethylene on Neutral, Anionic, and Cationic Gold Clusters”. In: J. Phys. Chem. C 114.6 (Feb. 2010), pp. 2484–2493. issn: 1932-7447. doi: 10.1021/jp909505y.

[48] I. P. Silverwood et al. “Evidence for a surface gold hydride on a nanostructured gold catalyst”. In: Chem. Commun. 52.3 (Dec. 2015), pp. 533–536. issn: 1359-7345. doi: 10.1039/C5CC06118K.

[49] Maela Manzoli et al. “Hydrogen interaction with gold nanoparticles and clusters supported on different oxides: A FTIR study”. In: Catal. Today 181.1 (Feb. 2012), pp. 62–67. issn: 0920-5861. doi: 10.1016/j.cattod.2011.07.029.

[50] Nicholas E. Singh-Miller and Nicola Marzari. “Surface energies, work functions, and surface relaxations of low-index metallic surfaces from first principles”. In: Phys. Rev. B 80.23 (Dec. 2009), p. 235407. doi: 10.1103/PhysRevB.80.235407.

[51] Yohaselly Santiago-Rodrıguez et al. “Atomic and molecular adsorption on Au(111)”. In: Surf. Sci. 627 (Sept.2014), pp. 57–69. issn: 0039-6028. doi: 10.1016/j.susc.2014.04.012.

[52] G. Kresse and J. Furthmuller. “Efficient iterative schemes for ab initio total-energy calculations using a plane-wave basis set”. In: Phys. Rev. B 54.16 (Oct.1996), pp. 11169–11186. doi: 10.1103/PhysRevB.54.11169.

[53] P. E. Blochl. “Projector augmented-wave method”. In: Phys. Rev. B 50.24 (Dec. 1994), pp. 17953–17979. doi:10.1103/PhysRevB.50.17953.

[54] G. Kresse and D. Joubert. “From ultrasoft pseudo potentials to the projector augmented-wave method”. In: Phys. Rev. B 59.3 (Jan. 1999), pp. 1758–1775. doi: 10.1103/PhysRevB.59.1758.

[55] John P. Perdew, Kieron Burke, and Matthias Ernzerhof. “Generalized Gradient Approximation Made Simple”. In: Phys. Rev. Lett. 77.18 (Oct. 1996), pp. 3865–3868. doi: 10.1103/PhysRevLett.77.3865.

[56] Stefan Grimme et al. “A consistent and accurate ab initio parametrization of density functional dispersion correction (DFT-D) for the 94 elements H-Pu”. In: J.Chem. Phys. 132.15 (Apr. 2010), p. 154104. issn: 0021-9606. doi: 10.1063/1.3382344.

View Article Online
DOI: 10.1039/D6NR01396A

[57] Shuichi Nosé. "A unified formulation of the constant temperature molecular dynamics methods". In: J.Chem. Phys. 81.1 (July 1984), pp. 511–519. issn: 0021-9606. doi: 10.1063/1.447334.

[58] William G. Hoover. "Canonical dynamics: Equilibrium phase-space distributions". In: Phys. Rev. A 31.3 (Mar.1985), pp. 1695–1697. doi: 10.1103/PhysRevA.31.1695.

[59] Min Yu and Dallas R. Trinkle. "Accurate and efficient algorithm for Bader charge integration". In: J. Chem.Phys. 134.6 (Feb. 2011), p. 064111. issn: 0021-9606. doi:10.1063/1.3553716.

View Article Online
DOI: 10.1039/D6NR01396A

Data availability

The computational data supporting this article have been deposited in Zenodo at [10.5281/zenodo.20509625]. The dataset includes the raw VASP input and output files for the DFT geometry optimizations, AIMD-derived quenched structures, electronic-structure calculations, and vibrational-frequency calculations discussed in the manuscript. The deposited files include INCAR, KPOINTS, CONTCAR, OSZICAR, OUTCAR, vasprun.xml, and DOSCAR files where applicable. POTCAR files are not redistributed.